

A fully automated method for 3D individual tooth identification and segmentation in dental CBCT

Tae Jun Jang, Kang Cheol Kim, Hyun Cheol Cho, and Jin Keun Seo

Abstract—Accurate and automatic segmentation of three-dimensional (3D) individual teeth from cone-beam computerized tomography (CBCT) images is a challenging problem because of the difficulty in separating an individual tooth from adjacent teeth and its surrounding alveolar bone. Thus, this paper proposes a fully automated method of identifying and segmenting 3D individual teeth from dental CBCT images. The proposed method addresses the aforementioned difficulty by developing a deep learning-based hierarchical multi-step model. First, it automatically generates upper and lower jaws panoramic images to overcome the computational complexity caused by high-dimensional data and the curse of dimensionality associated with limited training dataset. The obtained 2D panoramic images are then used to identify 2D individual teeth and capture loose- and tight- regions of interest (ROIs) of 3D individual teeth. Finally, accurate 3D individual tooth segmentation is achieved using both loose and tight ROIs. Experimental results showed that the proposed method achieved an F1-score of 93.35% for tooth identification and a Dice similarity coefficient of 94.79% for individual 3D tooth segmentation. The results demonstrate that the proposed method provides an effective clinical and practical framework for digital dentistry.

Index Terms—Cone-beam computerized tomography, digital dentistry, tooth segmentation, tooth identification, deep learning

I. INTRODUCTION

Digital dentistry is evolving rapidly along with the rapid innovation of artificial intelligence and the development of cone-beam computerized tomography (CT), intra-oral and face scanners, and dental three-dimensional (3D) printing. Digital dentistry enhances a dentist's efficiency and improves the accuracies of orthodontic diagnoses, treatment planning, and surgical guides. A fundamental component of digital dentistry is the 3D segmentation of teeth, jaws, and skulls from CBCT images. Moreover, accurate digital models of individual tooth geometry and jaws facilitate the simulation of prosthetic evaluation, cephalometric analysis, computer-aided digital implant planning, and bite irregularity prediction.

Automatic and accurate 3D individual tooth segmentation from CBCT images is a difficult task for the following reasons: (i) similar intensities between teeth roots and their surrounding alveolar bone; (ii) attached boundary between adjacent teeth in the crown parts.

Over the last decade, there have been several attempts to develop 3D tooth segmentation methods, most of which are based on level set methods [1]–[5]. Unfortunately, level set-based methods have fundamental limitations in achieving

fully automated segmentation. This difficulty arises from the dependence of such methods on the initialization of level set, and the automatic initialization is hindered by the complex image structure associated with adjacent teeth, the jaw, the alveolar bone, etc. Hence, user intervention through manual initialization is inevitable in this approach. Similarly, graph cut-based methods [6], [7] require manual intervention as the results are also affected by initialization. An anatomy-driven (or template-based) method [8] was proposed to automatically model the overall 3D tooth shape through B-spline representation. The disadvantage of this approach is its convex hull property, which causes inaccurate 3D tooth segmentation. Particularly, the approach is vulnerable to topological changes of molar teeth in transverse computerized tomography (CT) slices along the longitudinal axis.

Recently, deep learning methods have been applied in 3D tooth segmentation. Lee *et al.* [9] and Rao *et al.* [10] used a fully convolutional network (FCN) [11] for whole tooth segmentation instead of individual tooth segmentation. Chen *et al.* [12] attempted to provide individual tooth segmentation using a marker-controlled watershed transform from the tooth area predicted by FCN. The disadvantage of this approach is that a tooth may be broken into several fractions causing the watershed transform to assign several labels to an individual tooth. This drawback is a major obstacle to providing accurate and robust segmentation. Cui *et al.* [13] proposed a deep learning framework for individual tooth segmentation and identification using Mask R-CNN [14]. The limitation of these deep learning methods is patch-based approach to handle high-dimension inputs (*e.g.*, $800 \times 800 \times 400$ voxels in 3D CBCT image) and a limited amount of labeled samples. It is necessary to use both local and global information to achieve accurate segmentation with individual tooth identification. Thus, the drawback of this patch-based approach is its inability to reflect contextual (global) information, since each output of a convolutional network only depends on the corresponding patch.

Automatic individual tooth identification is also a difficult task. Recently, several individual tooth identification attempts [15], [16] have been made using convolutional networks. However, these approaches suffer from misclassification errors caused by adjacent teeth similarities.

Existing 3D tooth segmentation methods may not be effective for CBCT images that are severely corrupted by metal artifacts. In a clinical dental CBCT environment (*e.g.*, low dose radiation exposure), metal artifacts become common as the number of aged patients with metallic prosthesis increases. Hence, it would be desirable to develop a method that works

The authors are with School of Mathematics and Computing (Computational Science and Engineering), Yonsei University, Seoul, 03722.
E-mail: kangcheol@yonsei.ac.kr (corresponding author)

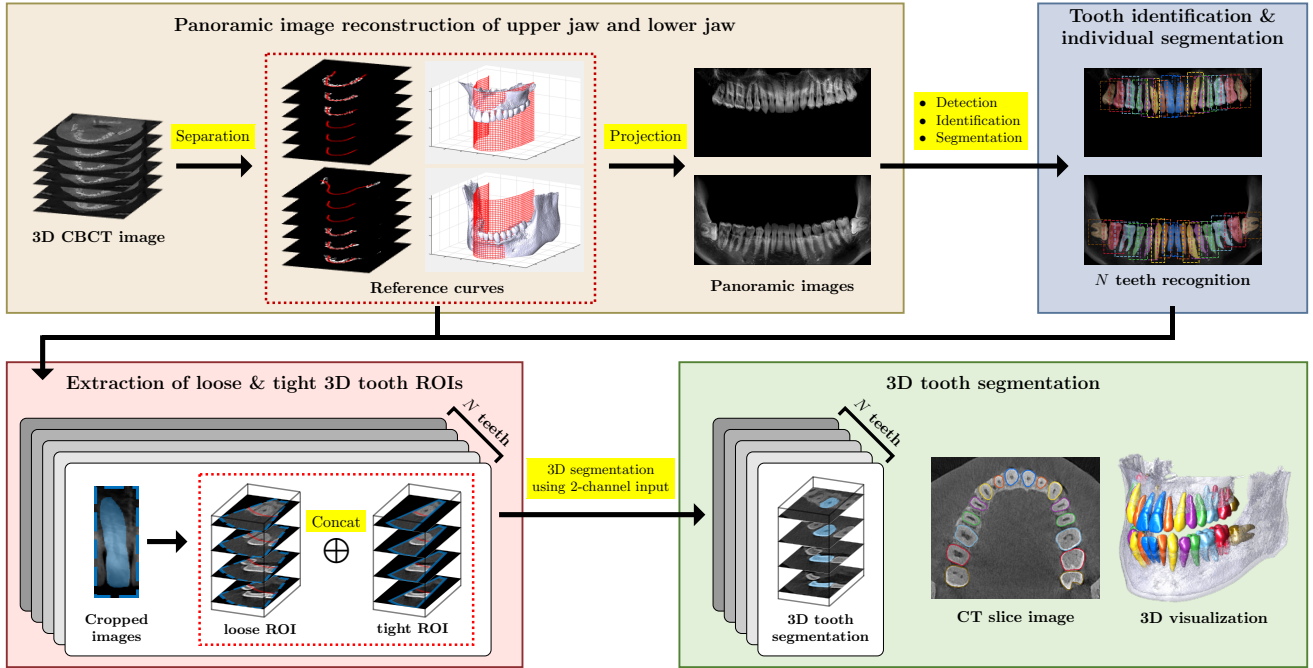


Fig. 1: Schematic diagram of the proposed method, which consists of four steps: 1) Panoramic image reconstruction of the upper and lower jaws from a 3D CBCT image; 2) tooth identification and 2D segmentation of individual teeth in the panoramic images; 3) extraction of loose and tight 3D tooth ROIs using the detected bounding boxes and segmented tooth regions; and 4) 3D segmentation for individual teeth from the 3D tooth ROIs.

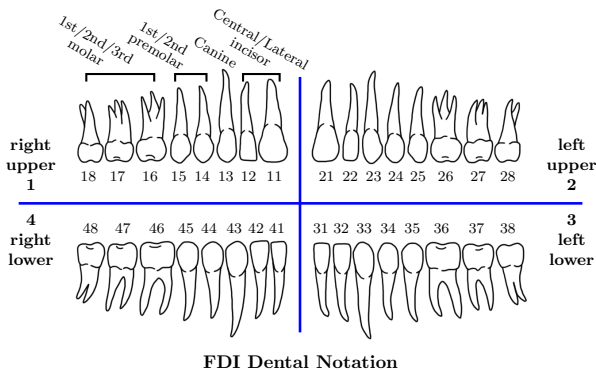


Fig. 2: Fédération Dentaire Internationale (FDI) dental notation using a two-digit numbering system. The first digit (quadrant code) represents a quadrant of teeth, and the second digit (tooth code) represents the order of the tooth from the central incisor in a quadrant.

well even in images degraded by metal artifacts.

This paper aimed to address these limitations by developing a hierarchical multi-step deep learning model. The proposed method is summarized as follows. The first step is to circumvent the high-dimensionality problem associated with CT images. This step automatically generates panoramic images of the upper and lower jaws from CT images where its size is smaller than the original CT image. The panoramic images of the upper and lower jaws are separated to reduce overlaps between adjacent teeth. Notably, panoramic images generated from CBCT images are not significantly affected

by metal-related artifacts. We utilize these panoramic images to accurately perform 2D tooth detection, identification, and segmentation. The second step is to identify individual teeth by two-digit numbers relative to their quadrant and location, as shown in Fig. 2. We develop a tooth detection method to localize bounding boxes that enclose each tooth and classifies them into four types according to tooth morphology. This method solve misclassification problems caused by similar adjacent teeth. The individual teeth are then identified using the results of tooth detection. Additionally, we perform 2D segmentation for individual teeth. The third step extracts loose and tight 3D tooth regions of interest (ROIs) from the 2D detected boxes and segmented tooth regions for accurate 3D individual tooth segmentation in the final step. Tight ROIs improve the segmentation accuracy. A schematic diagram of our method is described in Fig. 1.

The rest of this paper is organized as follows. The detail of the proposed method is described in Section II. Implementation details and experimental results are provided in Section III. Finally, Section IV presents the discussion and conclusion of this paper.

II. METHOD

Let \mathbf{X} denote a 3D CT image with voxel grid $\Omega := \{(x, y, z) \in \mathbb{N}^3 : 1 \leq x \leq N_x, 1 \leq y \leq N_y, 1 \leq z \leq N_z\}$, where N_x , N_y and N_z are the voxel sizes in directions x (sagittal axis), y (frontal axis) and z (longitudinal axis), respectively. We used CT images of size $800 \times 800 \times 400$. The value $\mathbf{X}(x, y, z)$ at the voxel position (x, y, z) is represented as the attenuation coefficient.

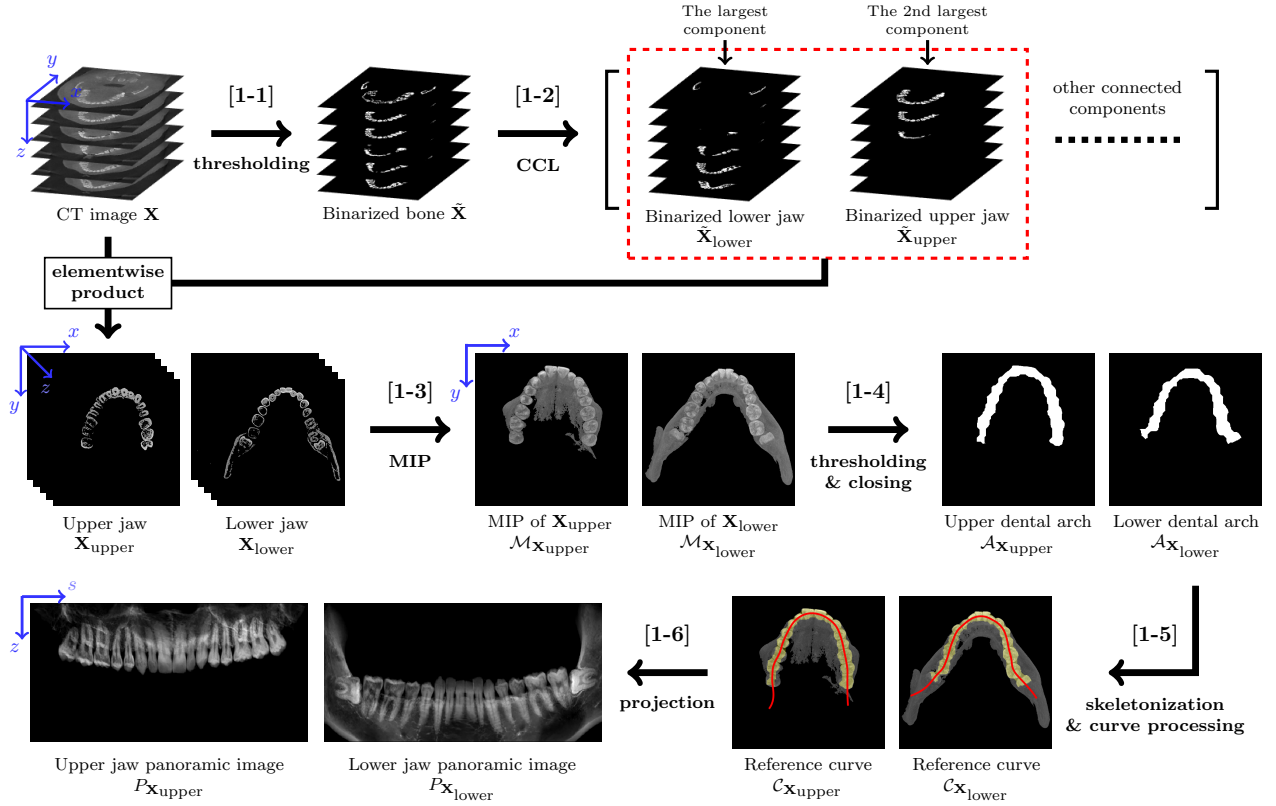


Fig. 3: Workflow of Step 1. This shows reconstruction process of upper jaw panoramic image $P_{X_{\text{upper}}}$ and low jaw panoramic images $P_{X_{\text{lower}}}$ from a 3D CT image X .

A. Step 1: Panoramic image reconstruction of the upper and lower jaws from a 3D CBCT image

This step describes the automatic reconstruction of panoramic images of the upper and lower jaws from a 3D CBCT image X . Fig. 3 illustrates the workflow.

[Step 1-1] To obtain a binary bone image \tilde{X} , a 3D CT image X is segmented into three classes (air, soft tissues, and bones) using multi-level version of Otsu's method [17]. The threshold values T_0 and T_1 for the histogram $h(t)$ corresponding to X are determined by

$$\{T_0, T_1\} = \underset{t_0, t_1}{\operatorname{argmax}} \left[\left(\frac{\sum_{0 \leq i < t_0} ip(i)}{\sum_{0 \leq i < t_0} p(i)} - \sum_{0 \leq i < t_0} p(i) \right)^2 + \left(\frac{\sum_{t_0 \leq i < t_1} ip(i)}{\sum_{t_0 \leq i < t_1} p(i)} - \sum_{t_0 \leq i < t_1} p(i) \right)^2 + \left(\frac{\sum_{i \geq t_1} ip(i)}{\sum_{i \geq t_1} p(i)} - \sum_{i \geq t_1} p(i) \right)^2 \right], \quad (1)$$

where $p(t) = h(t)/\sum h(i)$. The binary image $\tilde{X}(x, y, z)$ is 1 if $X(x, y, z) \geq \tilde{t}_i$, and 0 otherwise. As this value T_1 corresponds to an interface between soft tissues and bones, \tilde{X} can be viewed as a rough segmentation of upper and lower jaws.

[Step 1-2] Given the binary image \tilde{X} , we use the connected-component labeling (CCL) [18] technique to extract the upper jaw part (\tilde{X}_{upper}) and the lower jaw part (\tilde{X}_{lower}). The CCL

method generates all the connected components in a binary image. The lower jaw part is the largest connected component and the upper jaw part is the second largest connected component.

[Step 1-3] To create a 2D image M_{upper} displaying the upper dental arch, we apply maximum intensity projection (MIP) in the z direction to the grayscale upper jaw image ($X_{\text{upper}} = X \odot \tilde{X}_{\text{upper}}$, where \odot is an elementwise product), as follows:

$$M_{X_{\text{upper}}}(x, y) = \max_z X_{\text{upper}}(x, y, z). \quad (2)$$

Similarly, we obtain X_{lower} and $M_{X_{\text{lower}}}$ for the lower jaw.

[Step 1-4] Next, we obtain binary dental arch regions $A_{X_{\text{upper}}}$ and $A_{X_{\text{lower}}}$ by applying the Otsu's method [17] and the morphological closing operator [19] to the MIP images $M_{X_{\text{upper}}}$ and $M_{X_{\text{lower}}}$, respectively. Here, Otsu thresholding is adopted to get rough dental arch regions and the morphological closing operator is used to smoothen out the rough regions.

[Step 1-5] Given the upper dental arch region $A_{X_{\text{upper}}}$, we employ the morphological skeletonization [20] to extract a medial axis of the dental arch region. Cubic spline curve fitting, interpolation and extrapolation techniques are then applied to the medial axis, to obtain a smooth reference curve $C_{X_{\text{upper}}}$ passing through the dental arch region completely. The reference curve can be expressed as

$$C_{X_{\text{upper}}} = \{\mathbf{r}(s) = (x(s), y(s)) : s \in 1, 2, \dots, N_s\}, \quad (3)$$

where N_s is the number of curve points. Similarly, we can obtain $C_{X_{\text{lower}}}$ from the lower dental arch region $A_{X_{\text{lower}}}$.

[Step 1-6] As shown in Fig. 4, an upper jaw panoramic image is given by

$$P_{\mathbf{X}_{\text{upper}}}(s, z) = \int_{-\alpha}^{\alpha} \mathbf{X}_{\text{upper}}(\mathbf{r}(s) + t\mathbf{n}(s), z) dt, \quad (4)$$

where s is the parameter in (3), $\mathbf{r}(s) \in \mathcal{C}_{\mathbf{X}_{\text{upper}}}$, and $\mathbf{n}(s)$ is the unit normal vector at $\mathbf{r}(s)$. Similarly, we obtain the lower panoramic image $P_{\mathbf{X}_{\text{lower}}}$. For notational simplicity, we refer to both $P_{\mathbf{X}_{\text{upper}}}$ and $P_{\mathbf{X}_{\text{lower}}}$ as P .

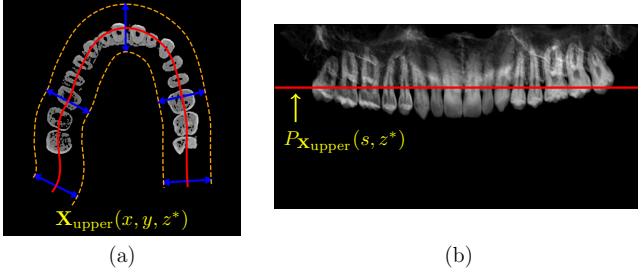


Fig. 4: Illustration of Step 1-6. (a) The z^* th slice of the upper jaw image $\mathbf{X}_{\text{upper}}$: the reference curve (red line), normal directions of the curve (blue arrow lines) and domain of projection (region inside orange dotted line). (b) Reconstructed panoramic image: the z^* th horizontal line of panoramic image $P_{\mathbf{X}_{\text{upper}}}$ corresponds to the z^* th slice.

B. Step 2: Bounding box detection, identification, and 2D segmentation of individual teeth in the reconstructed panoramic images

This step aims to identify and segment individual teeth in the reconstructed panoramic images. To achieve the goal, we first perform individual tooth detection. Here, the teeth are classified as incisor (class 1), canine (class 2), premolar (class 3), and molar (class 4).

[Step 2-1] To detect individual teeth in a panoramic image, we develop a deep learning method inspired by one-stage object detection [21], [22]. Given a panoramic image P with size $N_s \times N_z$ (e.g., $N_s \times N_z = 640 \times 320$), a uniform grid is created. Each grid cell G_{ij} is defined as follows:

$$G_{ij} = \{(s, z) \in \mathbb{N}^2 : g(i-1) < s \leq gi, \\ g(j-1) < z \leq gj\}, \quad (5)$$

where g is the length of grid cells. Then we learn a tooth detection map $f_{\text{det}} : P \mapsto Y$ that is given by

$$f_{\text{det}}(P) = \begin{pmatrix} Y_{1,1} & Y_{2,1} & \cdots & Y_{N_s,1} \\ Y_{1,2} & Y_{2,2} & \cdots & Y_{N_s,2} \\ \vdots & & \ddots & \vdots \\ Y_{1,N_z} & \cdots & \cdots & Y_{N_s,N_z} \end{pmatrix}, \quad (6)$$

where $Y_{ij} = (c_{ij}, \mathbf{b}_{ij}, \mathbf{p}_{ij})$ predicting a confidence score c_{ij} , a bounding box component \mathbf{b}_{ij} , and a class probability \mathbf{p}_{ij} in G_{ij} , as illustrated in Fig. 5. A confidence score $c_{ij} \in [0, 1]$ represents the existence of the tooth center in G_{ij} . A bounding box component is denoted by

$$\mathbf{b}_{ij} = (s_{ij}, z_{ij}, w_{ij}, h_{ij}). \quad (7)$$

where (s_{ij}, z_{ij}) is the center of the bounding box in G_{ij} , (w_{ij}, h_{ij}) indicates its width and height. For a tooth in the bounding box corresponding to \mathbf{b}_{ij} , we estimate a class probability

$$\mathbf{p}_{ij} = (p_{ij,1}, p_{ij,2}, p_{ij,3}, p_{ij,4}), \quad (8)$$

where $p_{ij,k}$ represents the probability of being tooth class k .

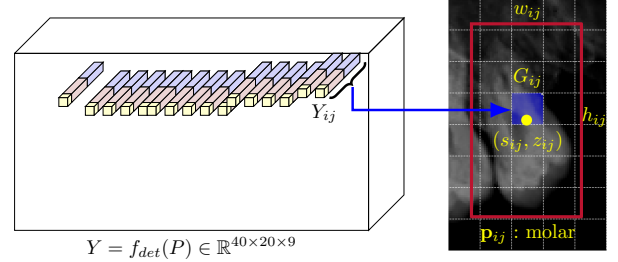


Fig. 5: Concept of Step 2-1. A detection map f_{det} predicts Y_{ij} for each G_{ij} . The center position in G_{ij} , the width and height of a bounding box, and the tooth class are expressed from Y_{ij} where the confidence score c_{ij} has a high value.

To find exact bounding boxes among the predicted boxes for all G_{ij} , we remove the boxes with scores $e_{ij} = c_{ij} * (\max_k p_{ij,k})$ less than 0.5. Several bounding boxes with high scores may appear near the center of a tooth. We adopt the non-maximal suppression (NMS) technique to filter out bounding boxes that highly overlap high-scoring boxes.

Using a labeled training dataset $\{(P^{(n)}, Y^{*(n)})\}_{n=1}^N$ where Y^* is ground truth, f_{det} is learned by minimizing the loss between the output $Y = f_{\text{det}}(P)$ and ground truth Y^* as follows:

$$\sum_{n=1}^N [\mathcal{L}_{\text{obj}}(Y^{(n)}, Y^{*(n)}) + \lambda_1 \mathcal{L}_{\text{noobj}}(Y^{(n)}, Y^{*(n)}) \\ + \lambda_2 \mathcal{L}_{\text{box}}(Y^{(n)}, Y^{*(n)}) + \mathcal{L}_{\text{cls}}(Y^{(n)}, Y^{*(n)})], \quad (9)$$

where

$$\mathcal{L}_{\text{obj}}(Y, Y^*) := \sum_{(i,j) \in \{(i,j) | c_{ij}^* = 1\}} (1 - c_{ij})^2, \quad (10)$$

$$\mathcal{L}_{\text{noobj}}(Y, Y^*) := \sum_{(i,j) \in \{(i,j) | c_{ij}^* = 0\}} (0 - c_{ij})^2, \quad (11)$$

$$\mathcal{L}_{\text{box}}(Y, Y^*) := \sum_{(i,j) \in \{(i,j) | c_{ij}^* = 1\}} |\mathbf{b}_{ij}^* - \mathbf{b}_{ij}|^2, \quad (12)$$

$$\mathcal{L}_{\text{cls}}(Y, Y^*) := \sum_{(i,j) \in \{(i,j) | c_{ij}^* = 1\}} \text{CrossEntropy}(\mathbf{p}_{ij}^*, \mathbf{p}_{ij}). \quad (13)$$

\mathcal{L}_{obj} , \mathcal{L}_{box} , and \mathcal{L}_{cls} represent the prediction errors for the confidence scores, bounding box components, and class probabilities where objects exist ($c_{ij}^* = 1$), respectively. $\mathcal{L}_{\text{noobj}}$ is related to the confidence scores where no objects exist ($c_{ij}^* = 0$). Since there is no object in most grid cells, the confidence score tends to be predicted as zero [21]. To eliminate the imbalance, $\mathcal{L}_{\text{noobj}}$ and \mathcal{L}_{box} are multiplied by constants $\lambda_1 = 0.1$ and $\lambda_2 = 5$, respectively.

Here, for a stable learning of bounding box regression [23], \mathbf{b}_{ij} is replaced by $\hat{\mathbf{b}}_{ij} = (\hat{s}_{ij}, \hat{z}_{ij}, \hat{w}_{ij}, \hat{h}_{ij})$ which satisfies the following conditions:

$$\begin{aligned} s_{ij} &= g(\hat{s}_{ij} + i - 1), & z_{ij} &= g(\hat{z}_{ij} + j - 1), \\ w_{ij} &= a_w \exp(\hat{w}_{ij}), & h_{ij} &= a_h \exp(\hat{h}_{ij}). \end{aligned} \quad (14)$$

where a_w and a_h are the width and height of an anchor box, respectively. We set a size of the anchor box as the mean size of the ground truth bounding boxes.

[Step 2-2] For each tooth in the detected bounding box, a number is assigned to identify the unique tooth according to the FDI system. For convenience, we first explain how the numbers are assigned to teeth in the upper jaw. As illustrated in Fig. 6, the detected bounding boxes are listed in ascending order of s coordinates of the box center. The upper right and upper left quadrants are divided from the middle of four sequential incisor boxes. For the two right incisors and the two left incisors, number 1 and 2 are assigned from the inside to the outside, respectively. Number 3 is assigned to the canines since there is only one in each quadrant. On each side, premolars are assigned numbers 4 and 5 from the inside to the outside. Likewise, molars are assigned numbers 6, 7 and 8 (if a wisdom tooth exists).

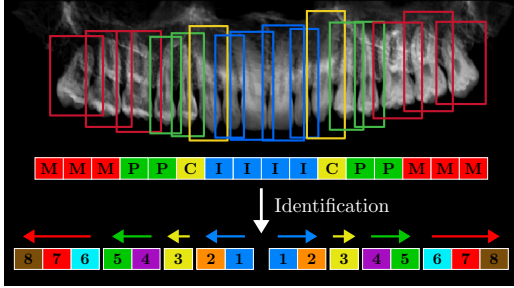


Fig. 6: Tooth identification process using the classification results in Step 2-1. The capital letters represent the first letters of the tooth type and the numbers are tooth codes.

[Step 2-3] The proposed 2D tooth segmentation method uses a U-shaped FCN [24] with taking advantage of bounding box knowledges obtained from Step 2-1. Let $S \in \mathbb{R}^{N_s \times N_z}$ denote the segmentation image for a tooth corresponding to a detected bounding box in P . We construct a training dataset $\{I_{\text{roi}}^{(n)}, Y_{\text{roi}}^{(n)}\}_{n=1}^N$ for individual teeth segmentation, where $I_{\text{roi}}^{(n)}$ and $Y_{\text{roi}}^{(n)}$ are tooth images of P and S cropped by the bounding boxes. A segmentation map $f_{\text{seg}} : I_{\text{roi}} \mapsto Y_{\text{roi}}$ is learned using a U-shaped network and minimizing the following loss:

$$\mathcal{L}_{\text{seg}} = \frac{1}{N} \sum_{n=1}^N \left[-\frac{1}{M} \sum_{\mathbf{x}} Y_{\text{roi}}^{(n)}(\mathbf{x}) \log \left[f_{\text{seg}} \left(I_{\text{roi}}^{(n)} \right) (\mathbf{x}) \right] \right], \quad (15)$$

where \mathbf{x} is a pixel position and M is the number of pixels of Y_{roi} .

C. Step 3: Extraction of loose and tight 3D tooth ROIs using the detected bounding boxes and segmented tooth regions

In this step, 3D tooth ROIs are obtained using the results of the previous steps. As described in Fig. 7, a bounding box

containing one tooth is projected back into the 3D CBCT image using (3) and (4). A loose ROI domain of the target tooth is then given by

$$D_{\text{box}} = \{(\mathbf{r}(s) + t\mathbf{n}(s), z) : -\alpha \leq t \leq \alpha, (s, z) \in B_{\text{box}}\}, \quad (16)$$

where B_{box} is the set of pixel positions in the bounding box. Similarly, a tight ROI domain D_{seg} is determined by B_{seg} , which is the set of pixel positions in the 2D tooth segmented region in the box.

The loose 3D tooth ROI \mathcal{R}_{box} is obtained by changing the voxel values outside D_{box} to 0, and extracting content in a 3D bounding box that fits closely around D_{box} , as shown in Fig. 7. Similarly, we obtain the tight 3D tooth ROI \mathcal{R}_{seg} by processing D_{seg} instead of D_{box} , and using the same 3D bounding box as above.

D. Step 4: 3D segmentation for individual teeth from the 3D tooth ROIs

In this final step, 3D individual tooth segmentation is performed by applying the loose ROI (\mathcal{R}_{box}) and tight ROI (\mathcal{R}_{seg}) to a 3D version of U-shaped FCN [24]. The tight ROI is crucial for improving the segmentation accuracy at the attached boundaries between a target tooth and its neighboring teeth.

The input of the network is $I_{\text{roi}3} = \mathcal{R}_{\text{box}} \oplus \mathcal{R}_{\text{seg}}$, which represents the concatenating vector of two ROIs. Let $Y_{\text{roi}3}$ denote a binary vector representing 3D tooth segmentation corresponding to $I_{\text{roi}3}$. Using a training dataset $\{I_{\text{roi}3}^{(n)}, Y_{\text{roi}3}^{(n)}\}_{n=1}^N$, we learn a 3D segmentation map $f_{\text{seg}3} : I_{\text{roi}3} \mapsto Y_{\text{roi}3}$ by minimizing the following loss:

$$\mathcal{L}_{\text{seg}3} = \frac{1}{N} \sum_{n=1}^N \left[-\frac{1}{V} \sum_{\mathbf{v}} Y_{\text{roi}3}^{(n)}(\mathbf{v}) \log \left[f_{\text{seg}3} \left(I_{\text{roi}3}^{(n)} \right) (\mathbf{v}) \right] \right], \quad (17)$$

where \mathbf{v} is a voxel position and V is the number of voxels $Y_{\text{roi}3}$.

III. EXPERIMENTS AND RESULTS

A. Dataset and implementation details

Experiments were conducted on 3D CT images produced by a dental CBCT with a circular trajectory (DENTRI-X; HDXWILL, Seoul, South Korea) using tube voltage 90kVp and tube current 10mA. All available datasets were formatted in the Digital Imaging and Communications in Medicine (DICOM) standard as a series of 16-bit grayscale images (corresponding to individual CT slices). The size of the original CBCT image was $800 \times 800 \times 400$, and its row and column pixel spacing and slice thickness were both 0.2mm. During scanning, a bite block was used to prevent contact between the upper and lower teeth.

We received 97 dental 3D CBCT images from HDXWILL. Using these data, we generated 194 upper jaw and lower jaw panoramic images in Step 1. We also received labeled data consisting of 97 2D individual tooth segmentation, bounding box components, and tooth codes, as well as 11 3D individual tooth segmentation. The labeling was performed by experts in HDXWILL.

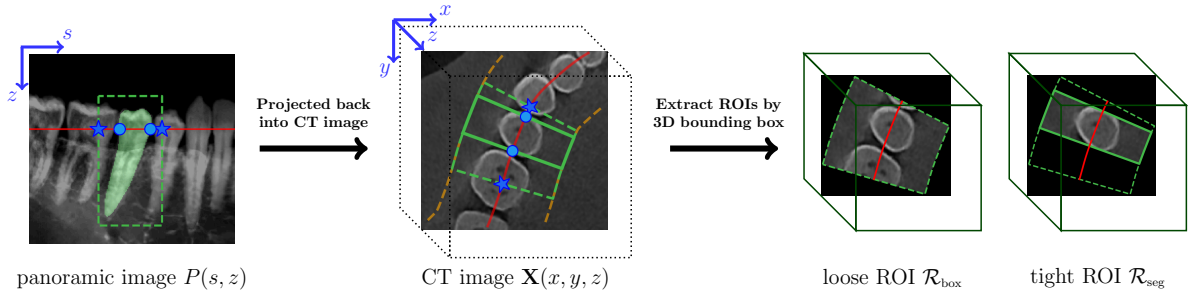


Fig. 7: Extraction of loose and tight 3D tooth ROIs. A loose ROI domain (green dotted line in \mathbf{X}) is determined by the domain of projection between points (blue stars in \mathbf{X}) on the reference curve corresponding to points (blue stars in P) on the bounding box. A 3D bounding box is then obtained by closely fitting the loose ROI domain. A loose 3D tooth ROI \mathcal{R}_{box} is extracted by cropping the CT image \mathbf{X} by the 3D bounding box and by changing values of voxels outside the loose ROI domain to 0. Similarly, a tight 3D tooth ROI \mathcal{R}_{seg} is obtained from the 2D segmented tooth region.

To reconstruct panoramic images from CT images, we used (4) for 3D CBCT images using a tomographic reconstruction software TIGRE [25]. The size of all panoramic images was fixed at 640×320 . The width of the panoramic images was determined by 640 reference curve points. In step 1-5, those points are obtained by interpolating 500 points on the smooth skeleton and by extrapolating 70 points at each end of the curve. To completely cover the teeth at both ends, we extrapolated 70 points (approximately 13.3mm) taking into account the average size of the molars. The height size 320 was determined by removing 80 CT slices that do not contain teeth from the bottom.

For the 2D detection and segmentation in Step 2-1 and 2-3, 66 CBCT dataset were used for training and 31 dataset for testing. Because two panoramic images (upper and lower parts) are obtained from each CBCT image through Step 1, we use 132 labeled training data and 62 test data. Meanwhile, for the 3D segmentation in Step 4, 7 CBCT dataset were used for training and 4 dataset for testing. Since each patient has approximately 28 to 32 teeth, each CBCT image can provide approximately 28 to 32 training data for individual tooth segmentation. To be precise, we use 216 training data and 112 test data for the 3D segmentation in Step 4. In Step 2-3 and 4, 2D tooth images and 3D loose and tight ROIs were resized to 128×128 and $128 \times 128 \times 128$, respectively.

B. Training of the proposed network

Training was implemented using Pytorch [26] on a CPU (Intel(R) Core(TM) i7-9700K, 3.60GHz) and GPU (NVIDIA GTX-2070, 8GB) system. In Steps 2 and 4, we trained three networks; tooth detection, 2D individual tooth segmentation, and 3D individual tooth segmentation. The proposed neural networks were trained by minimizing losses in (9), (15), and (17) using Adam optimizer [27]. The network architectures were determined using five-fold cross validation on the training dataset. We used the batch normalization [28] to prevent overfitting. Each training in Steps 2-1, 2-3, and 4 used batch sizes of 8, 32, and 4, respectively. We also used data augmentation techniques including random contrast, random

brightness adjustment, horizontal flip, and rotation between -8° and 8° .

C. Evaluation and result of the proposed method

1) *Bounding box detection*: For a quantitative evaluation of the bounding box detection, we provide four precision-recall (PR) curves [29] and their average precision (AP) [29], as shown in Fig. 8. When the intersection of union (IOU) threshold value was 0.6, according to the PR curve, the precision tends to stay high as the recall increases, and the AP was 88.11%.

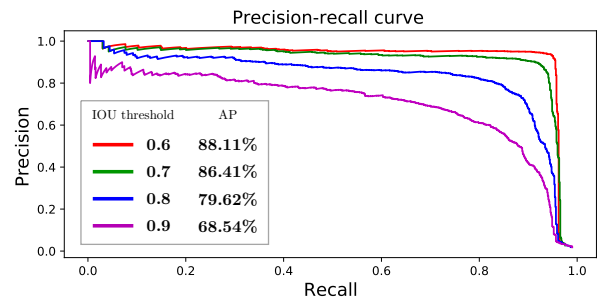


Fig. 8: Tooth detection results. A PR curve represents the change in the precision as the recall increases for a fixed IOU threshold value, which is used for NMS. The AP is the average of the precision values on a PR curve.

2) *Individual tooth identification*: This subsection presents the performance evaluation of tooth identification. The precision, recall, and F1-score were used to evaluate the results of the identification method. In Step 2-1, teeth are initially classified into four types, instead of directly predicting the eight tooth codes. The direct identification method can often misclassify teeth within the same tooth type. Fig. 9 summarizes the identification results for each tooth code. As shown in Fig. 9 (a), the direct method confuses first premolars (code 4) and wisdom teeth (code 8) in particular. These errors hinder the performance improvement of the direct method. However, the four type-based method achieves a high accuracy by preventing misclassification due to similar tooth shape. Table

It shows that the proposed method leads to more statistically accurate identification.

TABLE I: Quantitative evaluation for tooth identification methods.

Metric	Direct method	Proposed method
Precision (%)	93.05 \pm 7.85	96.81 \pm 1.67
Recall (%)	87.22 \pm 7.42	90.13 \pm 5.30
F1-score (%)	90.04 \pm 7.63	93.35 \pm 2.54

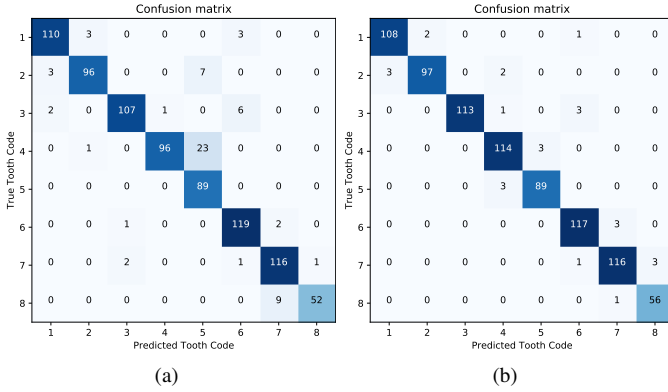


Fig. 9: Confusion matrix for tooth identification. The vertical and horizontal axes represent true tooth codes and predicted tooth codes, respectively. The diagonal components represent the number of correct identification. (a) Result of the direct method. (b) Result of the proposed method.

3) *Individual tooth segmentation*: In Steps 2-3 and 4, we performed the 2D and 3D individual tooth segmentation. To evaluate the segmentation performances, we used precision, recall, Dice similarity coefficient (DSC) [30], Hausdorff distance (HD) [31], and average symmetric surface distance (ASSD) [32].

2D individual tooth segmentation. The proposed method proceeds in two steps consisting of the bounding box detection in Step 2-1 and individual segmentation in Step 2-3, while Mask R-CNN [14] achieve the same task in a single step. We implemented both approaches, and the quantitative evaluation results are reported in Table I. The proposed method is numerically more accurate than the Mask R-CNN. In our experiment, the Mask R-CNN successfully detected teeth; however, there was a lack of segmentation detail at the edges of teeth, as shown in Fig. 10.

The accuracy of 2D segmentation is important because the key of precise 3D tooth segmentation is to use tight 3D tooth ROIs obtained by 2D segmentation. Although the detection and segmentation are not performed simultaneously, two simple convolutional networks (one-stage object detection and U-shaped FCN) are designed to achieve a high accuracy.

3D individual tooth segmentation. We developed a fully automated multi-step method for 3D individual segmentation. To verify the effectiveness of the proposed method, we compared it with patch-based Mask R-CNN [14] and ToothNet [13]. We also provided the segmentation results of the proposed method by adopting either loose or tight ROI, or both.

TABLE II: Quantitative evaluation for 2D tooth segmentation methods.

Metric	2D Mask R-CNN	Proposed method
Precision (%)	92.17 \pm 5.55	96.18 \pm 4.67
Recall (%)	90.35 \pm 5.87	93.17 \pm 5.83
DSC (%)	90.98 \pm 3.25	94.41 \pm 3.10
HD (mm)	1.64 \pm 0.93	1.34 \pm 0.86
ASSD (mm)	0.39 \pm 0.12	0.27 \pm 0.12

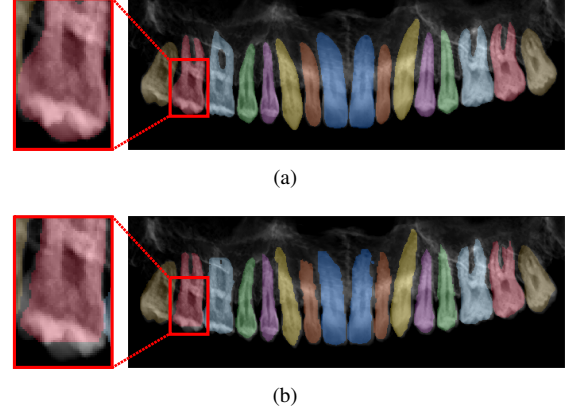


Fig. 10: Qualitative comparison of the proposed method and the Mask R-CNN. Segmentation results of (a) the proposed method and (b) Mask R-CNN. The Mask R-CNN is capable of tooth segmentation; however, there are some inaccuracies mainly at the edges of teeth.

Individual tooth segmentation can be formulated as an instance segmentation problem. Mask R-CNN is the state-of-the-art deep learning framework for instance segmentation. However, Mask R-CNN cannot be applied to large size 3D CBCT images directly because of the computational limit. For comparison experiments, we implemented Mask R-CNN in a patch-based fashion [33], [34] as an alternative to avoid the limitation. ToothNet is based on Mask R-CNN, which also adopts this approach. In the implementation, image patches had the size of $160 \times 160 \times 160$ and the stride between the patches was $40 \times 40 \times 40$. The patch-based approach yields redundant results by overlapping local image patches owing to the disconnected spatial relationship between adjacent patches. The integrated results are obtained by removing the overlapped segmentations according to ToothNet.

Patch-based 3D Mask R-CNN and ToothNet show lower segmentation performances in quantitative evaluation, as shown in Table III. These methods perform individual segmentation from the original CBCT images. In contrast, the proposed method has the advantage of using loose and tight ROIs that provide considerable background region in advance. In particular, the tight ROI excludes structures on sides (*e.g.*, adjacent teeth, jaw, etc) of the target tooth. To evaluate the effectiveness of the use of both loose and tight ROIs, we implemented experiments using either loose or tight ROI, or both on the same 3D segmentation network. When using only tight ROIs, the recall is the lowest because loss of tooth information may occur where the tight ROI boundary intersects the tooth boundary. The use of only loose ROI

TABLE III: Quantitative comparison for 3D tooth segmentation methods.

Metric	3D Mask R-CNN		ToothNet		Loose ROI		Tight ROI		Loose & tight ROIs mean \pm std
	mean \pm std	p -value	mean \pm std	p -value	mean \pm std	p -value	mean \pm std	p -value	
Precision (%)	93.98 \pm 11.07	< 0.001	89.40 \pm 5.84	< 0.001	94.80 \pm 6.53	< 0.001	94.70 \pm 2.79	< 0.001	95.97 \pm 2.00
Recall (%)	88.82 \pm 10.69	< 0.01	93.25 \pm 5.71	< 0.001	92.98 \pm 3.68	< 0.001	91.54 \pm 2.12	< 0.001	93.71 \pm 2.08
DSC (%)	90.75 \pm 10.48	< 0.001	91.40 \pm 5.07	< 0.001	93.76 \pm 4.81	< 0.001	92.98 \pm 1.75	< 0.001	94.79 \pm 1.34
HD (mm)	3.09 \pm 2.01	< 0.001	2.53 \pm 1.97	< 0.001	2.37 \pm 1.93	< 0.001	1.98 \pm 1.20	< 0.001	1.66 \pm 0.72
ASSD (mm)	0.36 \pm 0.31	< 0.001	0.27 \pm 0.20	< 0.001	0.20 \pm 0.20	< 0.001	0.19 \pm 0.05	< 0.001	0.14 \pm 0.04

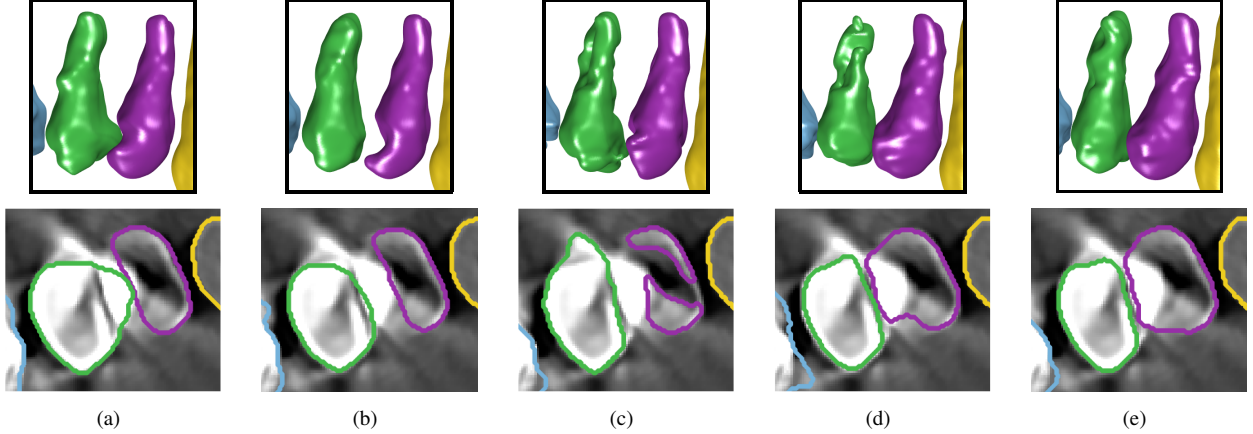


Fig. 11: Qualitative comparison for 3D individual tooth segmentation in a CBCT image with metal artifacts. Segmentation result of (a) Mask R-CNN, (b) ToothNet, (c) the proposed method using loose ROIs, (d) the proposed method using tight ROIs, and (e) the proposed method using both loose and tight ROIs.

containing tooth boundary shows a higher the recall. However, HD tends to be high because there is no information on tooth boundaries. A combination of the two ROIs enhances the segmentation performance, as the tight ROI provides detailed information on the target tooth and the loose ROI compensates for the disadvantage of the tight ROI.

Wilcoxon signed-rank test [35] is used to calculate the statistical significance differences between the proposed method and other methods, as summarized in Table III.

D. Metal artifact-contaminated CBCT

The proposed method effectively handles problems that are caused by metal-related artifacts. Fig. 12 shows that the CBCT image is significantly contaminated by metal artifacts, whereas metal artifacts are significantly reduced in the corresponding panoramic image generated by the CBCT image. The panoramic image in Step 1 allow to accurately perform 2D tooth detection and segmentation. These results provides prior knowledge of each 3D tooth as loose and tight ROIs. As shown in Fig. 12, the tight ROI excludes adjacent teeth, even though the tooth boundaries are obscured by metal artifacts. Fig. 11 provides a qualitative evaluation for 3D tooth segmentation in a CBCT image with metal artifacts. As shown in Fig. 11 (d) and (e), the segmentation results in the degraded CT image are superior to those of Fig. 11 (a)-(c) as the tight ROIs provide robust boundary information. However, Fig. 11 (d) presents that using only the tight ROIs may not provide robust segmentation because it can cut out the edges of the teeth. Therefore, Fig. 11 (e) illustrates the advantages and

effectiveness of the proposed method using both loose and tight ROIs.

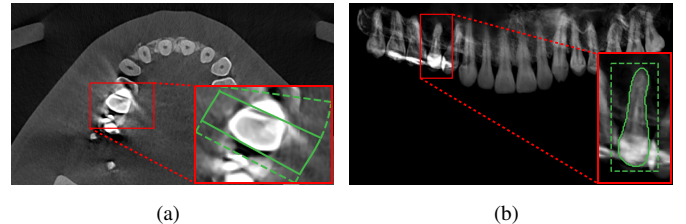


Fig. 12: (a) CBCT image affected by metal artifacts. (b) panoramic image generated from Step 1, which is not affected by metal artifacts. In (a), the green solid line represents the outline of the tight ROI obtained from the segmented region in (b). The tight ROI provide boundary information for the target tooth.

E. Special cases

This subsection shows the experimental results for the abnormal data (*e.g.*, missing tooth and implants). These are often encountered in real clinical practice.

1) *Missing teeth*: People often lose their teeth due to factors such as cavities, periodontal disease, aging, dental trauma and orthodontic treatment. To address these cases, we applied CBCT images with missing teeth (except for wisdom teeth) to our method. Four type-based classification was successful, but tooth identification was incomplete. With exception of canines,

each tooth quadrant contains two or more teeth of the same type. When numbering the neighboring tooth of the same type as a missing tooth, it is difficult to identify the neighboring tooth in panoramic images. Therefore, we suggest to perform only classification in the case of a missing tooth, as shown in Fig. 13.

2) *Implants*: Implant surgery is a dental prosthetic treatment to replace a missing tooth. An implant appears as a screw in a panoramic image, which is a unique signature. Although these data containing implants are totally unseen during model training, Fig. 14 shows successful bounding box detection and segmentation for implants. When applied to 3D segmentation, we also confirmed successful outcomes, as shown in Fig. 14. However, alternative implants cannot be predicted with original tooth classes since these have a different shape. This can be inferred from the classification and identification of neighboring teeth.

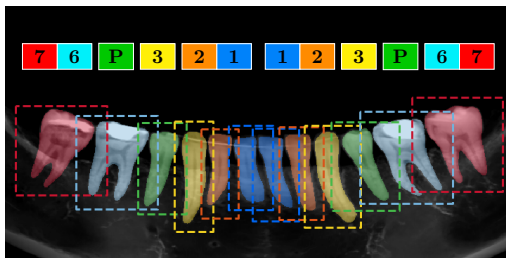


Fig. 13: Illustration of tooth identification when there is a missing tooth. Two premolar (class P) corresponding to number 4 are missing. It is not possible to determine whether the remaining premolar is number 4 or 5 by panoramic image alone. Hence, we suggest only marking the tooth type.

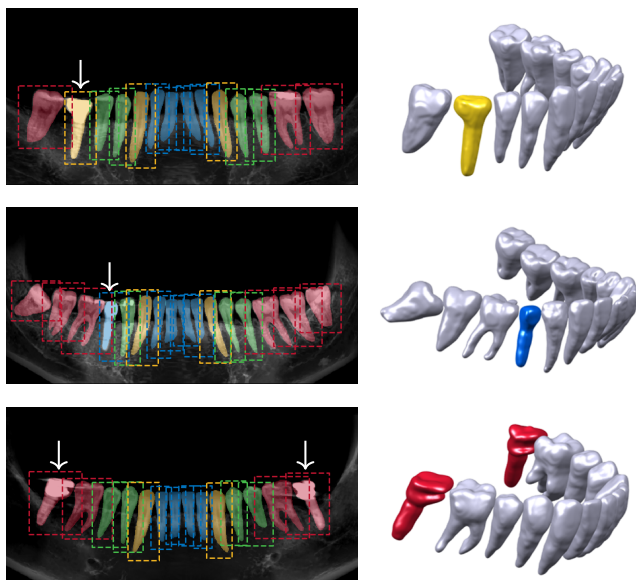


Fig. 14: Results of three CT images with implants. Implants were successfully segmented in both the panoramic image and 3D CT image. But, the implants are classified into different classes.

IV. DISCUSSION AND CONCLUSION

In this paper, we developed a fully automated segmentation and identification method for individual teeth and jaws from CBCT images. Given CBCT data, the method automatically generates the maxillary and mandibular panoramic images that are projected along the reference curve representing a region-based shape feature of a dental arch. In the maxillary and mandibular panoramic images, 2D tooth segmentation and identification are performed using deep learning methods, which are vital in high-precision 3D tooth segmentation and identification. Experiments showed that the accuracy of the method is suitable for the clinical setting. Our method overcomes the limitations of existing automated methods by achieving fully automation and improved accuracy. Additionally, the method addresses the difficulty of learning high-dimensional data.

The main idea of the proposed method is the careful use of the accurate and robust 2D tooth segmentation and identification in 2D panoramic images in an indirect manner to address the difficulty of 3D segmentation from metal artifact-contaminated 3D CBCT images. In a clinical dental CBCT environment (*e.g.*, low dose radiation exposure), metal related-artifacts are common. The proposed method utilizes the crucial observation that metal artifacts are significantly reduced in the upper and lower panoramic images generated from the CBCT images. The outcome in Step 2 serves as strong prior knowledge of 3D tooth segmentation, which plays an important role in separating teeth from 3D images, in cases where teeth are often contacted, overlapped, or connected owing to metal-related artifacts.

The automated system proposed in this study improves the efficiency of dentists by reducing the cumbersome and time-consuming manual intervention. The result provides an improved workflow for dentists to simulate pre-operative orthodontic treatment and manufacture implant surgical guides. Digital occlusion analysis is potentially possible by combining our method with the intra-oral scan model [36], [37] via registration. Hence, it is expected to play an important role in digital dentistry.

ACKNOWLEDGEMENTS

This research was supported by a grant of the Korea Health Technology R&D Project through the Korea Health Industry Development Institute (KHIDI), funded by the Ministry of Health & Welfare, Republic of Korea (HI20C0127). We would like to express our deepest gratitude HDXWILL which shares dental CBCT images and ground-truth data.

REFERENCES

- [1] H. Gao and O. Chae, "Individual tooth segmentation from ct images using level set method with shape and intensity prior," *Pattern Recognition*, vol. 43, no. 7, pp. 2406–2417, 2010.
- [2] Y. Gan, Z. Xia, J. Xiong, Q. Zhao, Y. Hu, and J. Zhang, "Toward accurate tooth segmentation from computed tomography images using a hybrid level set model," *Medical physics*, vol. 42, no. 1, pp. 14–27, 2015.
- [3] H.-T. Yau, T.-J. Yang, and Y.-C. Chen, "Tooth model reconstruction based upon data fusion for orthodontic treatment simulation," *Computers in biology and medicine*, vol. 48, pp. 8–16, 2014.

- [4] D. X. Ji, S. H. Ong, and K. W. C. Foong, "A level-set based approach for anterior teeth segmentation in cone beam computed tomography images," *Computers in biology and medicine*, vol. 50, pp. 116–128, 2014.
- [5] Y. Wang, S. Liu, G. Wang, and Y. Liu, "Accurate tooth segmentation with improved hybrid active contour model," *Physics in Medicine & Biology*, vol. 64, no. 1, p. 015012, 2018.
- [6] L. Hiew, S. Ong, K. W. Foong, and C. Weng, "Tooth segmentation from cone-beam ct using graph cut," in *Proceedings of the Second APSIPA Annual Summit and Conference*, 2010, pp. 272–275.
- [7] J. Keustermans, D. Vandermeulen, and P. Suetens, "Integrating statistical shape models into a graph cut framework for tooth segmentation," in *International Workshop on Machine Learning in Medical Imaging*. Springer, 2012, pp. 242–249.
- [8] S. Barone, A. Paoli, and A. V. Razonale, "Ct segmentation of dental shapes by anatomy-driven reformation imaging and b-spline modelling," *International journal for numerical methods in biomedical engineering*, vol. 32, no. 6, p. e02747, 2016.
- [9] S. Lee, S. Woo, J. Yu, J. Seo, J. Lee, and C. Lee, "Automated cnn-based tooth segmentation in cone-beam ct for dental implant planning," *IEEE Access*, vol. 8, pp. 50507–50518, 2020.
- [10] Y. Rao, Y. Wang, F. Meng, J. Pu, J. Sun, and Q. Wang, "A symmetric fully convolutional residual network with dcrf for accurate tooth segmentation," *IEEE Access*, vol. 8, pp. 92028–92038, 2020.
- [11] J. Long, E. Shelhamer, and T. Darrell, "Fully convolutional networks for semantic segmentation," in *Proceedings of the IEEE conference on computer vision and pattern recognition*, 2015, pp. 3431–3440.
- [12] Y. Chen, H. Du, Z. Yun, S. Yang, Z. Dai, L. Zhong, Q. Feng, and W. Yang, "Automatic segmentation of individual tooth in dental cbct images from tooth surface map by a multi-task fcn," *IEEE Access*, 2020.
- [13] Z. Cui, C. Li, and W. Wang, "Toothnet: automatic tooth instance segmentation and identification from cone beam ct images," in *Proceedings of the IEEE Conference on Computer Vision and Pattern Recognition*, 2019, pp. 6368–6377.
- [14] K. He, G. Gkioxari, P. Dollár, and R. Girshick, "Mask r-cnn," in *Proceedings of the IEEE international conference on computer vision*, 2017, pp. 2961–2969.
- [15] Y. Miki, C. Muramatsu, T. Hayashi, X. Zhou, T. Hara, A. Katsumata, and H. Fujita, "Classification of teeth in cone-beam ct using deep convolutional neural network," *Computers in biology and medicine*, vol. 80, pp. 24–29, 2017.
- [16] D. V. Tuzoff, L. N. Tuzova, M. M. Bornstein, A. S. Krasnov, M. A. Kharchenko, S. I. Nikolenko, M. M. Sveshnikov, and G. B. Bednenko, "Tooth detection and numbering in panoramic radiographs using convolutional neural networks," *Dentomaxillofacial Radiology*, vol. 48, no. 4, p. 20180051, 2019.
- [17] N. Otsu, "A threshold selection method from gray-level histograms," *IEEE transactions on systems, man, and cybernetics*, vol. 9, no. 1, pp. 62–66, 1979.
- [18] H. Samet and M. Tamminen, "Efficient component labeling of images of arbitrary dimension represented by linear bintrees," *IEEE transactions on pattern analysis and machine intelligence*, vol. 10, no. 4, pp. 579–586, 1988.
- [19] R. M. Haralick, S. R. Sternberg, and X. Zhuang, "Image analysis using mathematical morphology," *IEEE transactions on pattern analysis and machine intelligence*, no. 4, pp. 532–550, 1987.
- [20] T.-C. Lee, R. L. Kashyap, and C.-N. Chu, "Building skeleton models via 3-d medial surface axis thinning algorithms," *CVGIP: Graphical Models and Image Processing*, vol. 56, no. 6, pp. 462–478, 1994.
- [21] J. Redmon, S. Divvala, R. Girshick, and A. Farhadi, "You only look once: Unified, real-time object detection," in *Proceedings of the IEEE conference on computer vision and pattern recognition*, 2016, pp. 779–788.
- [22] W. Liu, D. Anguelov, D. Erhan, C. Szegedy, S. Reed, C.-Y. Fu, and A. C. Berg, "Ssd: Single shot multibox detector," in *European conference on computer vision*. Springer, 2016, pp. 21–37.
- [23] R. Girshick, J. Donahue, T. Darrell, and J. Malik, "Rich feature hierarchies for accurate object detection and semantic segmentation," in *Proceedings of the IEEE conference on computer vision and pattern recognition*, 2014, pp. 580–587.
- [24] O. Ronneberger, P. Fischer, and T. Brox, "U-net: Convolutional networks for biomedical image segmentation," in *International Conference on Medical image computing and computer-assisted intervention*. Springer, 2015, pp. 234–241.
- [25] A. Biguri, M. Dosanjh, S. Hancock, and M. Soleimani, "Tigre: a matlab-gpu toolbox for cbct image reconstruction," *Biomedical Physics & Engineering Express*, vol. 2, no. 5, p. 055010, 2016.
- [26] A. Paszke, S. Gross, F. Massa, A. Lerer, J. Bradbury, G. Chanan, T. Killeen, Z. Lin, N. Gimelshein, L. Antiga *et al.*, "Pytorch: An imperative style, high-performance deep learning library," in *Advances in neural information processing systems*, 2019, pp. 8026–8037.
- [27] D. P. Kingma and J. Ba, "Adam: A method for stochastic optimization," *arXiv preprint arXiv:1412.6980*, 2014.
- [28] S. Ioffe and C. Szegedy, "Batch normalization: Accelerating deep network training by reducing internal covariate shift," *arXiv preprint arXiv:1502.03167*, 2015.
- [29] M. Everingham, L. Van Gool, C. K. Williams, J. Winn, and A. Zisserman, "The pascal visual object classes (voc) challenge," *International journal of computer vision*, vol. 88, no. 2, pp. 303–338, 2010.
- [30] S. Rueda, S. Fathima, C. L. Knight, M. Yaqub, A. T. Papageorghiou, B. Rahmatullah, A. Foi, M. Maggioni, A. Pepe, J. Tohka *et al.*, "Evaluation and comparison of current fetal ultrasound image segmentation methods for biometric measurements: a grand challenge," *IEEE Transactions on medical imaging*, vol. 33, no. 4, pp. 797–813, 2013.
- [31] P. F. Raudaschl, P. Zaffino, G. C. Sharp, M. F. Spadea, A. Chen, B. M. Dawant, T. Albrecht, T. Gass, C. Langguth, M. Lüthi *et al.*, "Evaluation of segmentation methods on head and neck ct: auto-segmentation challenge 2015," *Medical physics*, vol. 44, no. 5, pp. 2020–2036, 2017.
- [32] O. Maier, B. H. Menze, J. von der Gablentz, L. Häni, M. P. Heinrich, M. Liebrand, S. Winzeck, A. Basit, P. Bentley, L. Chen *et al.*, "Isles 2015-a public evaluation benchmark for ischemic stroke lesion segmentation from multispectral mri," *Medical image analysis*, vol. 35, pp. 250–269, 2017.
- [33] D. Ciresan, A. Giusti, L. M. Gambardella, and J. Schmidhuber, "Deep neural networks segment neuronal membranes in electron microscopy images," in *Advances in neural information processing systems*, 2012, pp. 2843–2851.
- [34] B. Kim, K. C. Kim, Y. Park, J.-Y. Kwon, J. Jang, and J. K. Seo, "Machine-learning-based automatic identification of fetal abdominal circumference from ultrasound images," *Physiological measurement*, vol. 39, no. 10, p. 105007, 2018.
- [35] F. Wilcoxon, "Individual comparisons by ranking methods," in *Breakthroughs in statistics*. Springer, 1992, pp. 196–202.
- [36] X. Xu, C. Liu, and Y. Zheng, "3d tooth segmentation and labeling using deep convolutional neural networks," *IEEE transactions on visualization and computer graphics*, vol. 25, no. 7, pp. 2336–2348, 2018.
- [37] S. Tian, N. Dai, B. Zhang, F. Yuan, Q. Yu, and X. Cheng, "Automatic classification and segmentation of teeth on 3d dental model using hierarchical deep learning networks," *IEEE Access*, vol. 7, pp. 84817–84828, 2019.

APPENDIX A VISUALIZATION OF THE RESULT

In this section, we provide the qualitative evaluation of the four selected subjects by visualizing the results in each step. Fig. 15 presents the results for Step 2 using the upper and lower panoramic images generated by Step 1. Fig. 16 shows the individual tooth segmentation results. The results are displayed on three CBCT slices for each subject. Fig. 17 shows the visualized 3D teeth with a skull segmented from the CBCT image. The segmented regions of the teeth are filled in different colors according to the corresponding number.

APPENDIX B DEEP LEARNING NETWORK ARCHITECTURES

This section shows the architectures of the proposed three networks in Steps 2-1, 2-3 and 4. The architecture of tooth detection network is described as Table IV. On the last layer, different activation functions are used to predict confidence scores, bounding box components, and class probabilities at the same time. Table V shows the network of 2D tooth segmentation, which is a typical U-Net [24] structure. As shown in Table VI, 3D tooth segmentation network is also based on the U-Net structure.

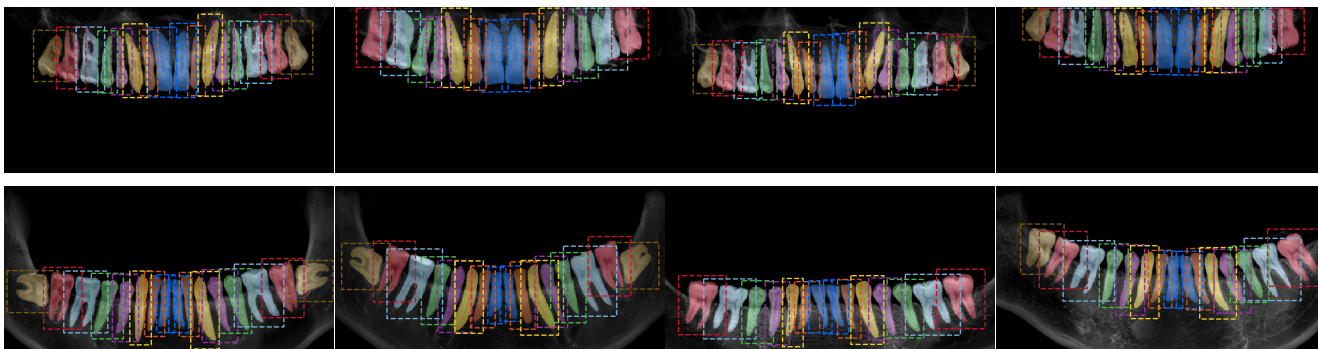


Fig. 15: Results of the proposed method for Step 2.

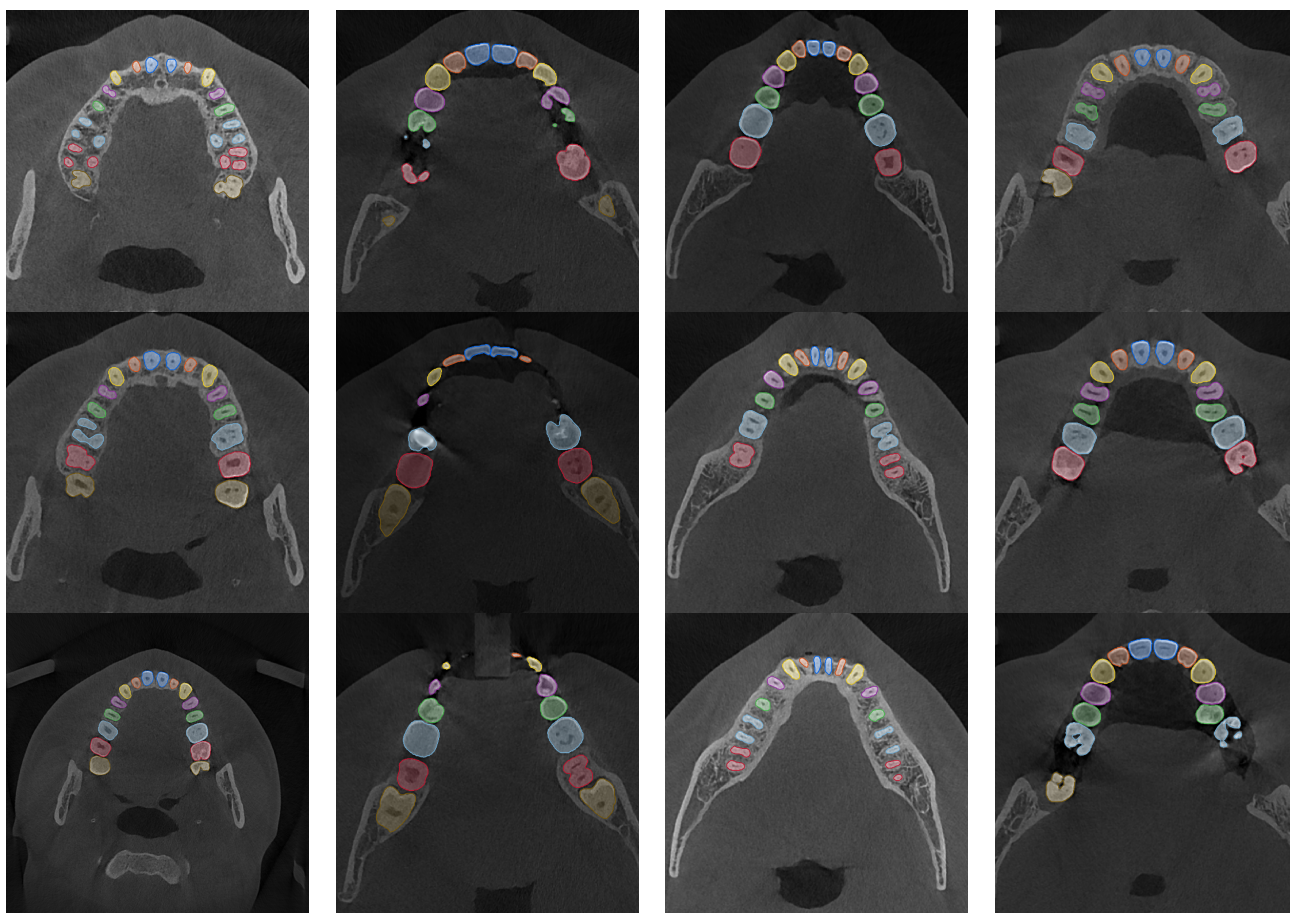


Fig. 16: 3D tooth segmentation results of the proposed method for four subjects.



Fig. 17: Visualization of 3D tooth segmentation results for four subjects.

TABLE IV: Network architecture of tooth detection in Step 2-1.

Layer	Input	Output	Kernel	Activation
conv($\times 2$) 1	$640 \times 320 \times 1$	$640 \times 320 \times 64$	$3^2 \times 64$	ReLU
max_pool 1	$640 \times 320 \times 64$	$320 \times 160 \times 64$	2^2	-
conv($\times 2$) 2	$320 \times 160 \times 64$	$320 \times 160 \times 128$	$3^2 \times 128$	ReLU
max_pool 2	$320 \times 160 \times 128$	$160 \times 80 \times 128$	2^2	-
conv($\times 3$) 3	$160 \times 80 \times 128$	$160 \times 80 \times 256$	$3^2 \times 256$	ReLU
max_pool 3	$160 \times 80 \times 256$	$80 \times 40 \times 256$	2^2	-
conv($\times 3$) 4	$80 \times 40 \times 256$	$80 \times 40 \times 512$	$3^2 \times 512$	ReLU
max_pool 4	$80 \times 40 \times 512$	$40 \times 20 \times 512$	2^2	-
conv($\times 1$) 5	$40 \times 20 \times 512$	$40 \times 20 \times 9$	$3^2 \times 9$	ReLU
conv($\times 1$) 6	$40 \times 20 \times 9$	$40 \times 20 \times 9$	$3^2 \times 9$	ReLU
conv($\times 1$) 7	$40 \times 20 \times 1$	$40 \times 20 \times 1$	$1^2 \times 1$	Sigmoid
	$40 \times 20 \times 2$	$40 \times 20 \times 2$	$1^2 \times 2$	Sigmoid
	$40 \times 20 \times 2$	$40 \times 20 \times 2$	$1^2 \times 2$	-
	$40 \times 20 \times 4$	$40 \times 20 \times 4$	$1^2 \times 4$	Softmax

TABLE V: Network architecture of 2D tooth segmentation in Step 2-3.

	Layer	Input	Output	Kernel	Activation
Encoding path	conv($\times 2$) 1	$128^2 \times 1$	$128^2 \times 64$	$3^2 \times 64$	ReLU
	max_pool 1	$128^2 \times 64$	$64^2 \times 64$	2^2	-
	conv($\times 2$) 2	$64^2 \times 64$	$64^2 \times 128$	$3^2 \times 128$	ReLU
	max_pool 2	$64^2 \times 128$	$32^2 \times 128$	2^2	-
	conv($\times 2$) 3	$32^2 \times 128$	$32^2 \times 256$	$3^2 \times 256$	ReLU
	max_pool 3	$32^2 \times 256$	$16^2 \times 256$	2^2	-
	conv($\times 2$) 4	$16^2 \times 256$	$16^2 \times 512$	$3^2 \times 512$	ReLU
Decoding path	upsample 1	$16^2 \times 512$	$32^2 \times 512$	2^2	-
	conv($\times 1$) 5	$32^2 \times 512$	$32^2 \times 256$	$3^2 \times 256$	ReLU
	concat with conv($\times 2$) 3	$32^2 \times 256$	$32^2 \times 512$	-	-
	conv($\times 2$) 6	$32^2 \times 256$	$32^2 \times 256$	$3^2 \times 256$	ReLU
	upsample 2	$32^2 \times 256$	$64^2 \times 256$	2^2	-
	conv($\times 1$) 7	$64^2 \times 256$	$64^2 \times 128$	$3^2 \times 128$	ReLU
	concat with conv($\times 2$) 2	$64^2 \times 128$	$64^2 \times 256$	-	-
	conv($\times 2$) 8	$64^2 \times 256$	$64^2 \times 128$	$3^2 \times 128$	ReLU
	upsample 3	$64^2 \times 128$	$128^2 \times 128$	2^2	-
	conv($\times 1$) 9	$128^2 \times 128$	$128^2 \times 64$	$3^2 \times 64$	ReLU
	concat with conv($\times 2$) 1	$128^2 \times 64$	$128^2 \times 128$	-	-
	conv($\times 2$) 10	$128^2 \times 128$	$128^2 \times 64$	$3^2 \times 64$	ReLU
	conv($\times 1$) 11	$128^2 \times 64$	$128^2 \times 1$	$1^2 \times 1$	Softmax

TABLE VI: Network architecture of 3D tooth segmentation in Step4.

	Layer	Input	Output	Kernel	Activation
Encoding path	max_pool 1	$128^3 \times 2$	$64^3 \times 2$	2^3	-
	conv($\times 5$) 2	$64^3 \times 2$	$64^3 \times 16$	$3^3 \times 16$	ReLU
	max_pool 2	$64^3 \times 16$	$32^3 \times 16$	2^3	-
	conv($\times 5$) 3	$32^3 \times 16$	$32^3 \times 32$	$3^3 \times 32$	ReLU
	max_pool 3	$32^3 \times 32$	$16^3 \times 32$	2^3	-
	conv($\times 5$) 4	$16^3 \times 32$	$16^3 \times 64$	$3^3 \times 64$	ReLU
Decoding path	upsample 1	$16^3 \times 64$	$32^3 \times 64$	2^3	-
	conv($\times 1$) 5	$32^3 \times 64$	$32^3 \times 64$	$3^3 \times 64$	ReLU
	concat with conv($\times 5$) 3	$32^3 \times 32$	$32^3 \times 64$	-	-
	conv($\times 5$) 6	$32^3 \times 64$	$32^3 \times 32$	$3^3 \times 32$	ReLU
	upsample 2	$32^3 \times 32$	$64^3 \times 32$	2^3	-
	conv($\times 1$) 7	$64^3 \times 32$	$64^3 \times 16$	$3^3 \times 16$	ReLU
	concat with conv($\times 5$) 2	$64^3 \times 16$	$64^3 \times 32$	-	-
	conv($\times 5$) 8	$64^3 \times 32$	$64^3 \times 16$	$3^3 \times 16$	ReLU
	upsample 3	$64^3 \times 16$	$128^3 \times 16$	2^3	-
	conv($\times 1$) 9	$128^3 \times 16$	$128^3 \times 8$	$3^3 \times 8$	ReLU
conv($\times 1$) 10	$128^3 \times 8$	$128^3 \times 1$	$1^3 \times 1$	Softmax	